The point spread function of the human head and its implications for transcranial current stimulation

Jacek P Dmochowski, Marom Bikson and Lucas C Parra

Department of Biomedical Engineering, City College of New York, New York, NY 10031, USA

E-mail: jdmochowski@ccny.cuny.edu

Abstract

Rational development of transcranial current stimulation (tCS) requires solving the 'forward problem': the computation of the electric field distribution in the head resulting from the application of scalp currents. Derivation of forward models has represented a major effort in brain stimulation research, with model complexity ranging from spherical shells to individualized head models based on magnetic resonance imagery. Despite such effort, an easily accessible benchmark head model is greatly needed when individualized modeling is either undesired (to observe general population trends as opposed to individual differences) or unfeasible. Here, we derive a closed-form linear system which relates the applied current to the induced electric potential. It is shown that in the spherical harmonic (Fourier) domain, a simple scalar multiplication relates the current density on the scalp to the electric potential in the brain. Equivalently, the current density in the head follows as the spherical convolution between the scalp current distribution and the point spread function of the head, which we derive. Thus, if one knows the spherical harmonic representation of the scalp current (i.e. the electrode locations and current intensity to be employed), one can easily compute the resulting electric field at any point inside the head. Conversely, one may also readily determine the scalp current distribution required to generate an arbitrary electric field in the brain (the 'backward problem' in tCS). We demonstrate the simplicity and utility of the model with a series of characteristic curves which sweep across a variety of stimulation parameters: electrode size, depth of stimulation, head size and anode–cathode separation. Finally, theoretically optimal montages for targeting an infinitesimal point in the brain are shown.

(Some figures may appear in colour only in the online journal)

1. Introduction

Transcranial current stimulation (tCS) is the application of weak currents to the surface of the scalp to elicit modulation of neural activity (Nitsche and Paulus 2000, Priori 2003). One may argue that clinical findings of the therapeutic benefits of weak scalp currents (Nitsche *et al* 2008, Brunoni *et al* 2011) are outpacing the pursuit of a rigorous understanding of tCS mechanisms of action as well as a consolidated model of transcranial volume conduction.

To develop rational stimulation paradigms, it is pivotal to relate the distribution of the applied scalp currents to the resulting electric fields in the brain. To that end, computational 'forward' models of transcranial electrical brain stimulation are standard tools to relate externally controlled dose (electrode montage, shape, current/voltage) (Peterchev *et al* 2011) to the resulting neural current distribution which then yields cognitive/behavioral changes. The relationship between dose and brain current is not trivial, and as such, models allow rational experimental and clinical design when specific brain regions are to be targeted or avoided. Because of the limitations of other approaches, such as phantoms (where tissue complexity cannot be accounted for) and imaging (where functional changes cannot be directly related to current flow), forward models, which are based on well-established physics (e.g. Ohm's law), are the standard tool in such an analysis (Miranda *et al* 2006, Holdefer *et al* 2006, Wagner *et al* 2007, Datta *et al* 2009). The complexity of forward models ranges from concentric spherical shells to high-resolution magnetic resonance imaging (MRI)-based individualized models, but regardless of complexity the purpose of these models remains to provide guidance and analysis to clinical protocols. Even as increasingly detailed models have been developed, simulations using concentric spheres have been used to explore basic dose approaches. It is precisely because individual anatomical idiosyncrasies influence current flow that spheres provide a basis for general exploration. However, finite-element (FE) numerical approaches are required for anatomically detailed models, either numerical or analytical approaches can be used with spheres. Numerical simulation requires the case-by-case analysis, significant computational resources and long computational times; on the other hand, analytical solutions offer the promise of an immediate solution which can be evaluated on any region of support (not just individual mesh points), exploration across the parameter space, derivation of general rules (trends) and the existence of a freely-available, benchmark forward model.

Previous analytical effort by Stecker (2005) into solving the forward model in tCS has yielded complex (lengthy) expressions not amenable to easy dissemination or implementation. More importantly, the frequency–domain linear system formulation of the problem, which drastically simplifies the solution, has gone unrecognized. Here, we formulate a straightforward linear system relating the applied scalp current to the resulting electric potential in the head. We operate in the spherical harmonic domain (i.e. spatial frequency) which leads to a scalar transfer between the scalp current density and brain electric potential. Moreover, by transforming the solution back to the space domain, we derive the point spread function (PSF) of the human head, which represents the 'response' of the head to a unit-mass point of input current.

We demonstrate the simplicity and utility of the proposed model by conducting an analysis of the effect of electrode size, followed by a comparison of the induced electric field in the adult brain versus that of a child, as well as an investigation into the role of anode–cathode separation on the resulting current flow. Additionally, we arrive at an elegant solution to the 'backward problem' in tCS: given a desired electric field in the brain, to derive the corresponding scalp current density. It is shown that in the asymptotic limit (infinite current), any electric field which possesses a spherical harmonic expansion may be physically realized by a corresponding scalp current density distribution which may be computed with our model. To that end, we compute the idealized montage for the case of a delta-Dirac function (an electric field which has a

nonzero value only at a single point in the brain), representing the optimal montage for focal stimulation.

Our overall goal is to present a rigorous yet accessible model that can serve as a benchmark for future effort. For readers that would prefer to omit the mathematical development while still absorbing the main results, we suggest to browse the figure captions and then continue directly to the discussion, which summarizes the key results and discusses issues such as the relationship of spherical models to its complex MRI-based counterparts.

2. Problem formulation: quasi-static volume conduction

Consider a homogeneous volume conductor $\mathcal{V}$. Under the 'quasi-static' assumption—Ohm's law is valid and one can ignore electromagnetic induction (Nunez and Srinivasan 2006)—the electric potential inside $\mathcal{V}$ is governed by Laplace's equation (Jackson 1975, Griffiths 1999):

$$\nabla^2 V = 0, \tag{1}$$

where ∇^2 is the Laplacian operator. In order to determine a unique solution to Laplace's equation within the volume of interest, one must specify either the potential on the boundary encasing the volume (Dirichlet boundary condition), or its normal derivative on the boundary (Neumann boundary condition). When encountering non-homogeneous conductors, such as the human head, one exploits continuity of electric potential and current across region boundaries to build up solutions for each homogenous section of the conductor. In the forthcoming tCS model, the boundaries that we will consider are spherical. Thus, it is convenient to rewrite Laplace's equation (1) in spherical co-ordinates (Jackson 1975, Griffiths 1999):

$$\nabla^2 V = \frac{1}{r^2} \frac{\partial}{\partial r} \left(r^2 \frac{\partial V}{\partial r} \right) + \frac{1}{r^2 \sin \theta} \frac{\partial}{\partial \theta} \left(\sin \theta \frac{\partial V}{\partial \theta} \right) + \frac{1}{r^2 \sin^2 \theta} \frac{\partial^2 V}{\partial \phi^2} = 0, \tag{2}$$

where r, θ and ϕ denote the range, elevation and azimuth, respectively, in a spherical co-ordinate system. While (2) may at first glance appear more complex than its Cartesian counterpart, it has a well-known general solution. Using the method of separation of variables, the solution is given by a linear combination of the *spherical harmonics* (Jackson 1975):

$$V(r, \theta, \phi) = \sum_{l=0}^{\infty} \sum_{m=-l}^{l} (A_{lm} r^l + B_{lm} r^{-(l+1)}) Y_{lm}(\theta, \phi), \tag{3}$$

where A_{lm} and B_{lm} denote the weighting coefficients of the basis functions

$$Y_{lm}(\theta, \phi) = \sqrt{\frac{2l+1}{4\pi} \frac{(l-m)!}{(l+m)!}} P_{lm}(\cos \theta)\, e^{im\phi}, \tag{4}$$

which are the complex-valued spherical harmonics, and P_{lm} is the associated Legendre polynomial of order l and degree m.

2.1. Spherical Fourier transform

Much like any function defined over the real numbers may be expressed in terms of complex exponentials, any function f defined on the surface of a sphere of radius R may be written as a linear combination of the spherical harmonics:

$$f(\theta, \phi) = \sum_{l=0}^{\infty} \sum_{m=-l}^{l} F_{lm} R^l Y_{lm}(\theta, \phi), \tag{5}$$

where the coefficients of the expansion are computed according to

$$F_{lm}R^l = \int_0^{2\pi} \int_0^\pi f(\theta, \phi)Y_{lm}^*(\theta, \phi) \sin\theta \, d\theta \, d\phi, \tag{6}$$

where * denotes complex conjugation. On the unit sphere, the R^l terms disappear from (5) and (6).

In the following section, we employ the spherical Fourier transform to derive an analytical solution to the forward and backward problems in tCS.

3. Linear system model and solution

We employ a four concentric spherical shell model to derive an analytical relationship between the applied scalp current and the resulting electric potential in the head. In order of distance from the origin, the concentric shells model the brain $\mathcal{V}_1$, the cerebrospinal fluid (CSF) $\mathcal{V}_2$, the skull $\mathcal{V}_3$ and the scalp $\mathcal{V}_4$. The radii of the shells are denoted by $R_i, i = 1, \ldots, 4$; the conductivities are denoted by $\sigma_i, i = 1, \ldots, 4$. The general solution for $\mathcal{V}_i$ is written as

$$V_i(r, \theta, \phi) = \sum_{l=0}^\infty \sum_{m=-l}^l \left(A_{lm}^{(i)}r^l + B_{lm}^{(i)}r^{-(l+1)}\right)Y_{lm}(\theta, \phi), \qquad i = 1, \ldots, 4, \tag{7}$$

with $B_{lm}^{(1)} = 0 \; \forall l, m$ as $\mathcal{V}_1$ includes the origin[1]. We are thus left with seven unknowns for each spherical harmonic lm. By differentiating (7) with respect to r, the radial derivative of potential in each shell follows as

$$\frac{\partial V_i}{\partial r} = \sum_{l=0}^\infty \sum_{m=-l}^l \left[lA_{lm}^{(i)}r^{l-1} - (l+1)B_{lm}^{(i)}r^{-(l+2)}\right]Y_{lm}(\theta, \phi), \qquad i = 1, \ldots, 4.$$

Owing to the continuity of the normal component of the current and the electric potential along tissue boundaries, we have the following (six) boundary conditions:

$$V_i(R_i, \theta, \phi) = V_{i+1}(R_i, \theta, \phi) \quad i = 1, 2, 3$$
$$\sigma_i \left(\frac{\partial V_i}{\partial r}\right)_{r=R_i} = \sigma_{i+1} \left(\frac{\partial V_{i+1}}{\partial r}\right)_{r=R_i} \quad i = 1, 2, 3.$$

To derive the final boundary condition, we make use of the fact that in tCS, the normal component of the current density on the scalp, denoted here by $J(\theta, \phi)$, is specified fully by the employed montage. Moreover, we employ the quasi-static expression for the electric field $\mathbf{E} = -\nabla V$ to express the radial component of electric field E on the scalp as

$$E(\phi, \theta) = -\frac{\partial V_4}{\partial r}. \tag{8}$$

Substituting Ohm's law $J = \sigma E$ into (8) yields

$$J(\theta, \phi) = -\sigma_4 \left(\frac{\partial V_4}{\partial r}\right)_{r=R_4}. \tag{9}$$

As $J(\theta, \phi)$ is defined on the surface of a sphere, it has a spherical Fourier representation:

$$J(\theta, \phi) = \sum_{l=0}^\infty \sum_{m=-l}^l J_{lm}R_4^l Y_{lm}(\theta, \phi), \tag{10}$$

---

[1] In order for the terms $B_{lm}^{(1)}r^{-(l+1)}$ to remain finite at $r = 0$, $B_{lm}^{(1)}$ must be zero.

with appropriate spherical harmonic coefficients J_{lm}. Due to the orthonormality of the spherical harmonics, all seven boundary conditions may be expressed in the frequency domain:

$$A_{lm}^{(i)} R_i^l + B_{lm}^{(i)} R_i^{-(l+1)} = A_{lm}^{(i+1)} R_i^l + B_{lm}^{(i+1)} R_i^{-(l+1)}, \quad i = 1, 2, 3,$$

$$\sigma_i \left[l A_{lm}^{(i)} R_i^{l-1} - (l+1) B_{lm}^{(i)} R_i^{-(l+2)} \right] = \sigma_{i+1} \left[l A_{lm}^{(i+1)} R_i^{l-1} - (l+1) B_{lm}^{(i+1)} R_i^{-(l+2)} \right], \quad i = 1, 2, 3,$$

$$-\sigma_4 \left[l A_{lm}^{(4)} R_4^{l-1} - (l+1) B_{lm}^{(4)} R_4^{-(l+2)} \right] = J_{lm} R_4^l, \tag{11}$$

and further written in matrix form as

$$\mathbf{J}_{lm} = \mathbf{H}_l \mathbf{V}_{lm}, \tag{12}$$

where

$$\mathbf{H}_l$$

$$= \begin{bmatrix} R_1^l & -R_1^l & -R_1^{-(l+1)} & 0 & 0 & 0 & 0 \\ \sigma_1 l R_1^{l-1} & -\sigma_2 l R_1^{l-1} & \sigma_2 (l+1) R_1^{-l-2} & 0 & 0 & 0 & 0 \\ 0 & R_2^l & R_2^{-(l+1)} & -R_2^l & -R_2^{-(l+1)} & 0 & 0 \\ 0 & \sigma_2 l R_2^{l-1} & -\sigma_2 (l+1) R_2^{-l-2} & -\sigma_3 l R_2^{l-1} & \sigma_3 (l+1) R_2^{-l-2} & 0 & 0 \\ 0 & 0 & 0 & R_3^l & R_3^{-(l+1)} & -R_3^l & -R_3^{-(l+1)} \\ 0 & 0 & 0 & \sigma_3 l R_3^{l-1} & -\sigma_3 (l+1) R_3^{-l-2} & -\sigma_4 l R_3^{l-1} & \sigma_4 (l+1) R_3^{-l-2} \\ 0 & 0 & 0 & 0 & 0 & -l \sigma_4 R_4^{-1} & (l+1) \sigma_4 R_4^{-2l-2} \end{bmatrix},$$

$$\mathbf{V}_{lm} = \begin{bmatrix} A_{lm}^{(1)} & A_{lm}^{(2)} & B_{lm}^{(2)} & A_{lm}^{(3)} & B_{lm}^{(3)} & A_{lm}^{(4)} & B_{lm}^{(4)} \end{bmatrix}^T$$

and

$$\mathbf{J}_{lm} = \begin{bmatrix} 0 & 0 & 0 & 0 & 0 & 0 & J_{lm} \end{bmatrix}^T.$$

The linear system of (12) relates the current density on the scalp ($\mathbf{J}_{lm}$) to the electric potential in the head ($\mathbf{V}_{lm}$) via the matrix $\mathbf{H}_l$, which is characterized by the geometry of the head and the electrical conductivities of the comprising tissues. Indeed, $\mathbf{H}_l$ is the transfer function of the head, specified in the spherical Fourier domain.

Equation (12) is a reflection of the physics governing the flow of current in tCS: the applied currents and resulting electric potentials are coupled by the linear system $\mathbf{H}_l$. It is interesting to point out, however, that given a vector of potentials in the head (i.e. $\mathbf{V}_{lm}$), multiplication by the transfer matrix $\mathbf{H}_l$ only yields a valid solution for the scalp currents if all elements of the corresponding vector $\mathbf{H}_l \mathbf{V}_{lm}$, with the exception of the last element, are zero.

More importantly, $\mathbf{H}_l$ is a full-rank matrix and thus possesses an inverse which we denote by $\mathbf{G}_l = \mathbf{H}_l^{-1}$. We then obtain the following relation:

$$\mathbf{V}_{lm} = \mathbf{G}_l \mathbf{J}_{lm}. \tag{13}$$

But $\mathbf{J}_{lm}$ only has one nonzero element: this means that, remarkably, the electric potentials inside the head may be written as a scalar multiple of the input current:

$$\begin{aligned} \text{brain:} \quad & A_{lm}^{(1)} = [\mathbf{G}_l]_{1,7} J_{lm} \\ \text{CSF:} \quad & A_{lm}^{(2)} = [\mathbf{G}_l]_{2,7} J_{lm}, \quad B_{lm}^{(2)} = [\mathbf{G}_l]_{3,7} J_{lm} \\ \text{skull:} \quad & A_{lm}^{(3)} = [\mathbf{G}_l]_{4,7} J_{lm}, \quad B_{lm}^{(3)} = [\mathbf{G}_l]_{5,7} J_{lm} \\ \text{scalp:} \quad & A_{lm}^{(4)} = [\mathbf{G}_l]_{6,7} J_{lm}, \quad B_{lm}^{(4)} = [\mathbf{G}_l]_{7,7} J_{lm} \end{aligned} \tag{14}$$

where $[\mathbf{G}_l]_{i,j}$ has been defined as the element in the ith row and jth column of $\mathbf{G}_l$. In the frequency domain, the relationship between the applied current density and the resulting electric potential in the brain is given by a simple scalar multiplication. This greatly facilitates
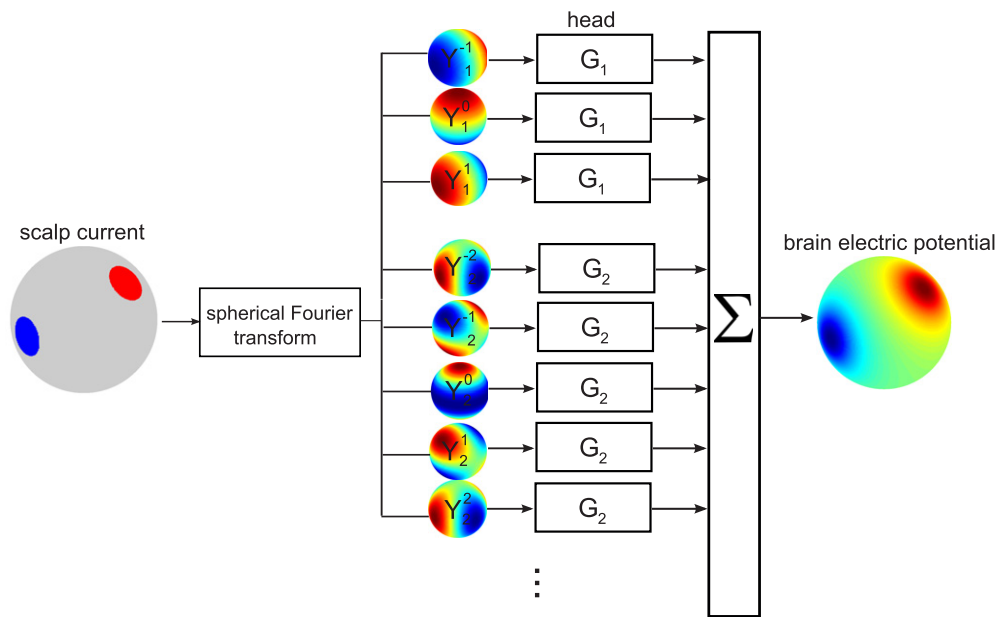
Figure 1. By expressing the applied scalp current in terms of orthonormal basis functions and deriving the head frequency response (G_l), the resulting current flow in the brain follows as a linear combination of the spherical harmonics $Y_{lm}(\theta, \phi)$.

the computation of the electric field given an electrode montage—the 'forward problem' in tCS.

The existence of an inverse for $\mathbf{H}_l$ also ensures that we can compute the scalp current distribution corresponding to a given electric potential in the brain:

$$J_{lm} = \frac{A_{lm}^{(1)}}{[\mathbf{G}_l]_{1,7}}, \tag{15}$$

which elegantly provides an instant solution to the 'backward problem' in tCS: the determination of the electrode montage which generates an arbitrary desired electric field.

Figure 1 illustrates the convenience of working in the spherical harmonic domain: the applied scalp current is expressed as a linear combination of orthonormal basis functions $Y_{lm}(\theta, \phi)$. By multiplying each frequency component with the corresponding head transfer function $[\mathbf{G}_l]_{1,7}$ (depicted by G_l in the figure) and then summing across all harmonics, we obtain the electric potential generated inside the brain.

4. Results

Below we demonstrate the utility of the results derived above.

4.1. Spatial frequency response of the head

The frequency response of a temporal filter represents the gain presented to a temporal sinusoid; similarly, the coefficients $[\mathbf{G}_l]_{i7}$, $i = 1, \ldots, 7$, convey the spatial frequency responses between the current density on the scalp and that inside the head. A subtle but important point is that the scalp current and current through the skull, CSF and brain reside on spheres of different radii. For example, to relate the applied scalp current to the radially oriented current density

in the brain, we have the following:

$$-\sigma_1 \left(\frac{\partial V_1}{\partial r} \right)_{r=R_1} = -\sigma_1 \sum_{l=0}^{\infty} \sum_{m=-l}^{l} A_{lm}^{(1)} l R_1^{l-1} Y_{lm}(\theta, \phi),$$

$$J(\theta, \phi) = \sum_{l=0}^{\infty} \sum_{m=-l}^{l} J_{lm} R_4^l Y_{lm}(\theta, \phi), \tag{16}$$

where the radial derivative of V_1 resides on a sphere of radius R_1, while J exists on a sphere of radius R_4. Thus, in order to compute a meaningful transfer (i.e. for the transfer to reflect a ratio of coefficients pertaining to the same basis function) between the applied scalp current and the current on the brain surface, one should compute

$$\text{scalp–brain: } G_l^{(1)} \triangleq \frac{-\sigma_1 A_{lm}^{(1)} l R_1^{l-1}}{J_{lm} R_4^l} = \frac{-\sigma_1 [\mathbf{G}_l]_{1,7} l R_1^{l-1}}{R_4^l}. \tag{17}$$

Similarly, we define the following:

$$\text{scalp–CSF: } G_l^{(2)} \triangleq \frac{-\sigma_2 \left(A_{lm}^{(2)} l R_2^{l-1} - B_{lm}^{(2)} (l+1) R_2^{-(l+2)} \right)}{J_{lm} R_4^l}$$

$$= \frac{-\sigma_2 \left([\mathbf{G}_l]_{2,7} l R_2^{l-1} - [\mathbf{G}_l]_{3,7} (l+1) R_2^{-(l+2)} \right)}{R_4^l},$$

$$\text{scalp–skull: } G_l^{(3)} \triangleq \frac{-\sigma_3 \left(A_{lm}^{(3)} l R_3^{l-1} - B_{lm}^{(3)} (l+1) R_3^{-(l+2)} \right)}{J_{lm} R_4^l}$$

$$= \frac{-\sigma_3 \left([\mathbf{G}_l]_{4,7} l R_3^{l-1} - [\mathbf{G}_l]_{5,7} (l+1) R_3^{-(l+2)} \right)}{R_4^l}. \tag{18}$$

Physically, the coefficients $G_l^{(1)}$, $G_l^{(2)}$ and $G_l^{(3)}$ represent the gain presented by the head to a scalp current defined by a spherical sinusoid $Y_{lm}(\phi, \theta)$ at the brain, CSF and skull, respectively. Figure 2(a) displays the spatial frequency responses between the scalp current and the radially oriented current at the surfaces of the skull, CSF and brain. The responses were computed by constructing $\mathbf{H}_l$ and taking its inverse $\mathbf{G}_l = \mathbf{H}_l^{-1}$. The following standard values (Nunez and Srinivasan 2006) were used for the computation $\{R_i\}_{i=1}^4 = \{0.08, 0.081, 0.086, 0.092\}$ m and $\{\sigma_i\}_{i=1}^4 = \{0.2, 1.65, 0.001, 0.465\}$ S m^{-1} and the responses are shown up to a spatial frequency $l = 140$ cycles/π. To elucidate the effect of including the CSF layer in the model, we also computed the frequency responses after setting $\sigma_2 = \sigma_1$, or by extending the brain to encompass the space previously occupied by the CSF.

As expected, the scalp–skull frequency response upper bounds the remaining responses. For all tissues, the transfer function is monotonically decreasing with frequency—indeed, the human head is a spatial low-pass filter, strongly attenuating input current distributions with spatial frequencies greater than 5 cycles/π. Note that the classical 'roll-off' of the low-pass filter is sharpest for the brain (0.61 dB per harmonic order) and slowest for the skull (0.29 dB per harmonic order). The greatest attenuation is posed by the skull, with the response dropping by 30 dB across the skull at 60 cycles/π. Moreover, the effect of including the thin CSF layer into the model is significant, adding approximately 13 dB of attenuation at 60 cycles/π.

4.2. PSF of the head

Note that in the frequency domain, the potential in the brain is given by a product of the applied current and the transfer $G_l^{(1)}$. Multiplication in the frequency domain corresponds to convolution in the space domain; indeed, the *spherical convolution* theorem (Driscoll and
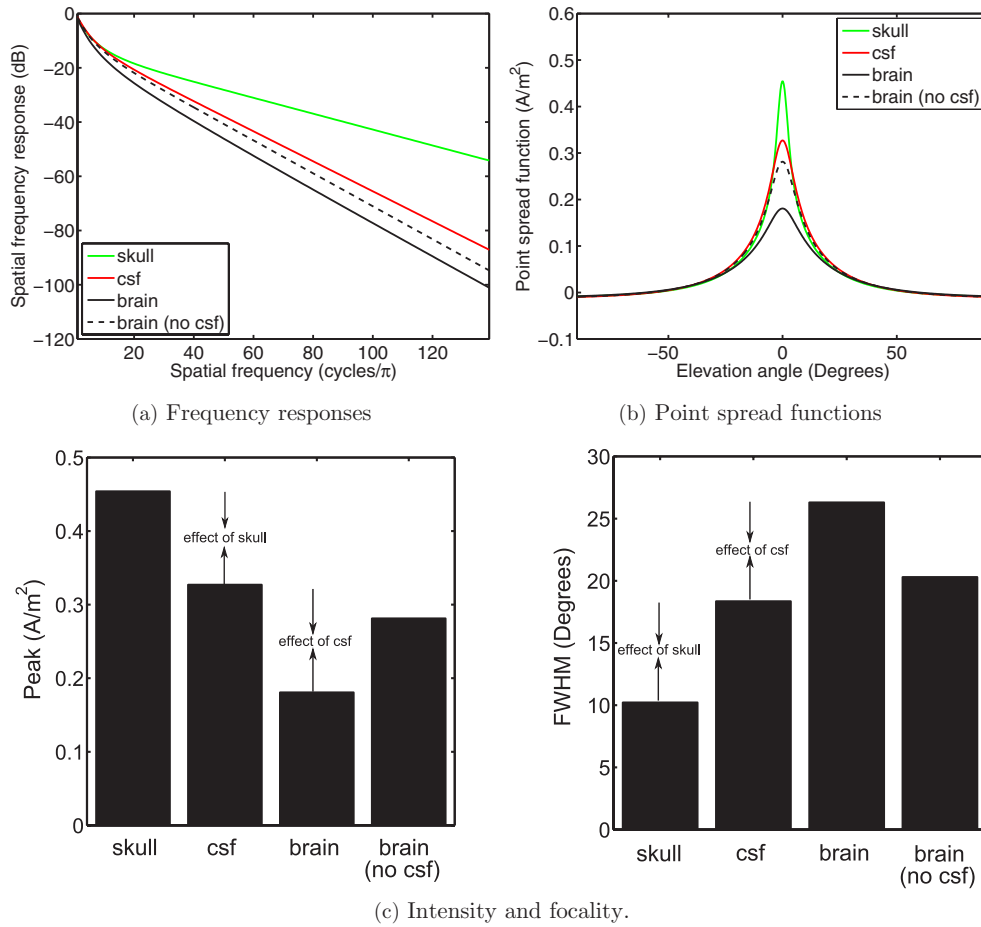
(a) Frequency responses

(b) Point spread functions

(c) Intensity and focality.

Figure 2. (a) Frequency responses: the spatial frequency responses between the current density applied at the scalp and that inside the head. The head is a low-pass spatial filter, strongly attenuating spherical sinusoids greater than $l = 5$. (b) Point spread functions: the corresponding PSFs, which represent the current density inside the head resulting from the application of a unit current at the surface of the scalp. (c) Intensity and focality: the peaks and FWHMs of the PSFs quantify the attenuating and blurring effects of the skull and CSF (shown as differences in adjacent bar height), while elucidating the importance of incorporating CSF in the head model.

Healy 1994) states that the spherical Fourier transform of a convolution of two functions defined on a sphere is given by a scaled product of their respective spherical harmonic coefficients:

$$u(\theta, \phi) * v(\theta, \phi) \Leftrightarrow 2\pi \sqrt{\frac{4\pi}{2l + 1}} U_l V_{lm}, \qquad (19)$$

where $*$ denotes convolution on the sphere. Moreover, we know that the inverse Fourier transform of a frequency response is the impulse response, or PSF in the case of two dimensions. Thus, by transforming the transfer functions of (17) and (18) into the space domain via (5), we may compute the PSF, which here represents the distribution of current density inside the head resulting from the application of an infinitely large, infinitesimally narrow unit current on the surface of the scalp at $\theta = \phi = 0$.

Figure 2(b) displays the PSFs corresponding to the surfaces of the skull, CSF and brain—note that due to the inherent azimuthal symmetry, the PSFs are depicted as a univariate function of the elevation angle. Moreover, the peaks and angular spreads of the PSFs are shown in figure 2(c), with the latter quantified in the form of the 'full-width half-max' (FWHM), or the angular spread at which the response drops to half of the peak. We also report the PSFs on the surface of the brain in the absence of CSF, as described above.

On the surface of the skull, the radial current peaks at 0.45 A m^{-2} and exhibits a FWHM of just 10°. The peak current drops to 0.33 A m^{-2} and 0.18 A m^{-2} on the surfaces of the CSF and brain, respectively, with the corresponding FWHMs rising to 18° and 26°. Thus, despite the CSF layer consisting of only a 1 mm thickness, its high conductivity results in a large diffusion of current. Consequently, not including the CSF layer in the model results in errors of 55% and 22% when estimating the peak current density and FWHM, respectively.

4.3. Modeling the effect of varying electrode size

The effect of electrode size on the resulting stimulation has been the subject of some investigation (Nitsche *et al* 2007, Miranda *et al* 2009). Intuitively, one expects the focality of the induced electric field to be greater when passing the applied current through electrodes of a limited spatial extent (this effect was verified indirectly in (Nitsche *et al* 2007)). On the other hand, the perceived skin sensation is amplified by using electrodes with a reduced surface area (Minhas *et al* 2010). To rigorously quantify the effect of the electrode size on the resulting electric field in the brain, we utilized the relationships derived above to compute a set of forward models corresponding to varying electrode sizes. We considered the classical motor montage targeting the primary motor cortex (M1), with the anode at electrode C3 of the standard 10/10 system for electrode placement (Chatrian *et al* 1985), and the return over the contralateral supraorbital region (electrode FP2). This montage is often referred to as 'M1-SO'. We computed the spherical harmonic coefficients of a spherical 'cap' (see the appendix) which represents a circular electrode with finite surface area, which ranged here from 5 to 25 cm^2. For all electrode sizes, the current density was selected to equalize the total current delivered to 2 mA. The results are shown in figure 3.

The spherical cap model is depicted in panel A: the angular extent of the nonzero region (white) was chosen such that the surface area of the electrode matches the desired size. Panel B displays the electric field magnitude in the brain (radially below the anode) as a function of depth into the volume. Smaller electrodes lead to an increase in field magnitude below the anode, with the effect waning as the depth into the brain volume increases: the field intensity curves converge to a common value at the center of the brain (8 cm depth). For each electrode size, the peak intensities are shown in panel C. A fivefold reduction in the surface area of the electrodes results in a 60% increase in the electric field below the anode. From panel D, it is evident that this increase in field intensity is also accompanied by increased spatial concentration of the field. Specifically, the FWHM decreases from 66° to 39° when decreasing the electrode area from 25 to 5 cm^2.

4.4. Modeling the effect of head size

One parameter of relevance and wide variation in the tCS population is head size. For example, it is important to accurately translate (i.e. scale down) typical adult tCS dosages to the smaller heads of children and to make reliable predictions of the nature of the electric field induced by tCS in children. We obtained sample anatomical MRI scans of one adult (male, age 35) and one child (male, age 12) which were manually segmented into the comprising tissue
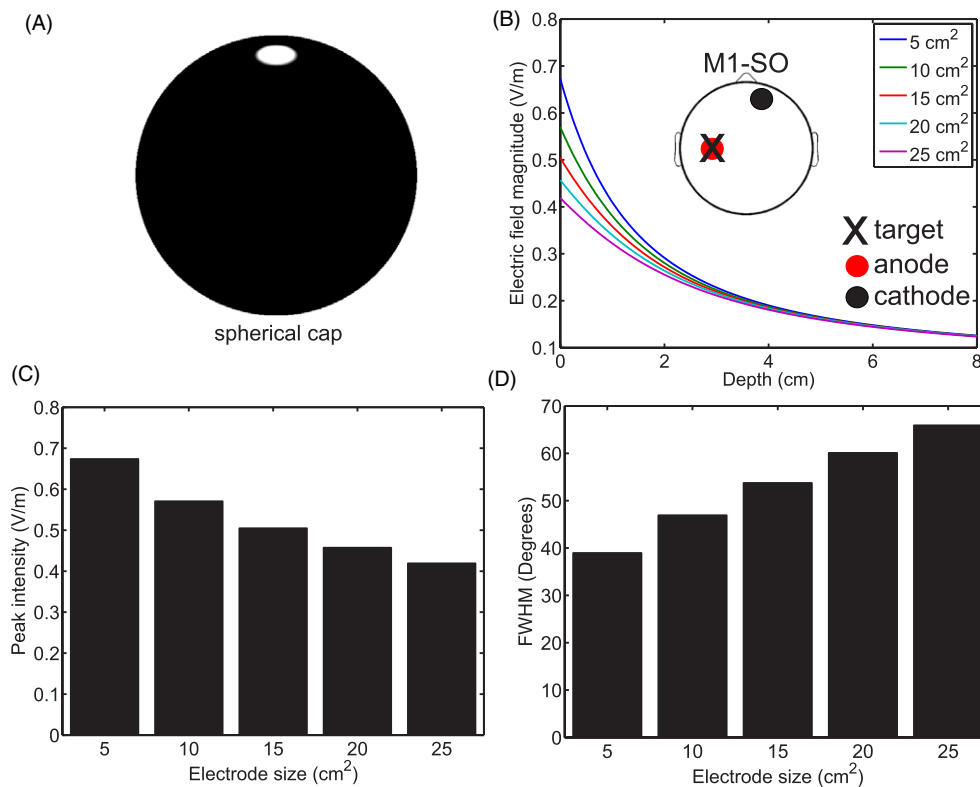
Figure 3. The effect of varying electrode surface area on the resulting electric field below the anode, which is situated above the primary motor cortex. (A) For each electrode size, the total current delivered is 2 mA and achieved by appropriately selecting the current density applied to a circular electrode modeled by a spherical cap. (B) Smaller electrodes lead to a higher intensity (measured directly below the anode), with the effect pronounced on the surface of the brain volume and waning as depth increases. (C) On the brain surface, a five-fold decrease in electrode surface area leads to a 60% increase in the electric field magnitude below the anode. (D) Moreover, this increased intensity is accompanied by greater focality, with a FWHM of 39° employing 5 cm^2 electrodes, compared to 66° at 25 cm^2.

types (scalp, skull, CSF, brain). The resulting binary masks were then employed to measure the thicknesses of the CSF (adult: 3.1 mm, child: 1.3 mm), skull (adult: 4.5 mm, child: 2.3 mm) and scalp (adult: 6.32 mm, child: 5.5 mm) underneath electrode Oz. The radius of the (spherical) head was computed by fitting the MRI head dimensions to a sphere. From this, the radius of the brain (adult: 80 mm, child: 73 mm) followed as the total of the scalp, skull and CSF thicknesses subtracted from the head radius. We then constructed four-shell models corresponding to the adult and the child. The standard conductivity values stated earlier were assigned to both head models. We then implemented two popular montages: the classic M1-SO montage with large 25 cm^2 electrodes, and the more focal '4×1' montage (Datta *et al* 2009) consisting of 1.13 cm^2 electrodes (anode over C3, and cathodes at FC1, FC5, CP1 and CP5, each carrying a quarter of the return current). For each head and montage, we computed the forward model corresponding to an anodal current of 2 mA.

Figure 4 depicts the electric field magnitude (radially below the anode) as a function of depth into the brain (A: M1-SO; B: 4×1). On the cortical surface, the induced field in the child brain has an intensity approximately double that of the adult in the case of the M1-SO
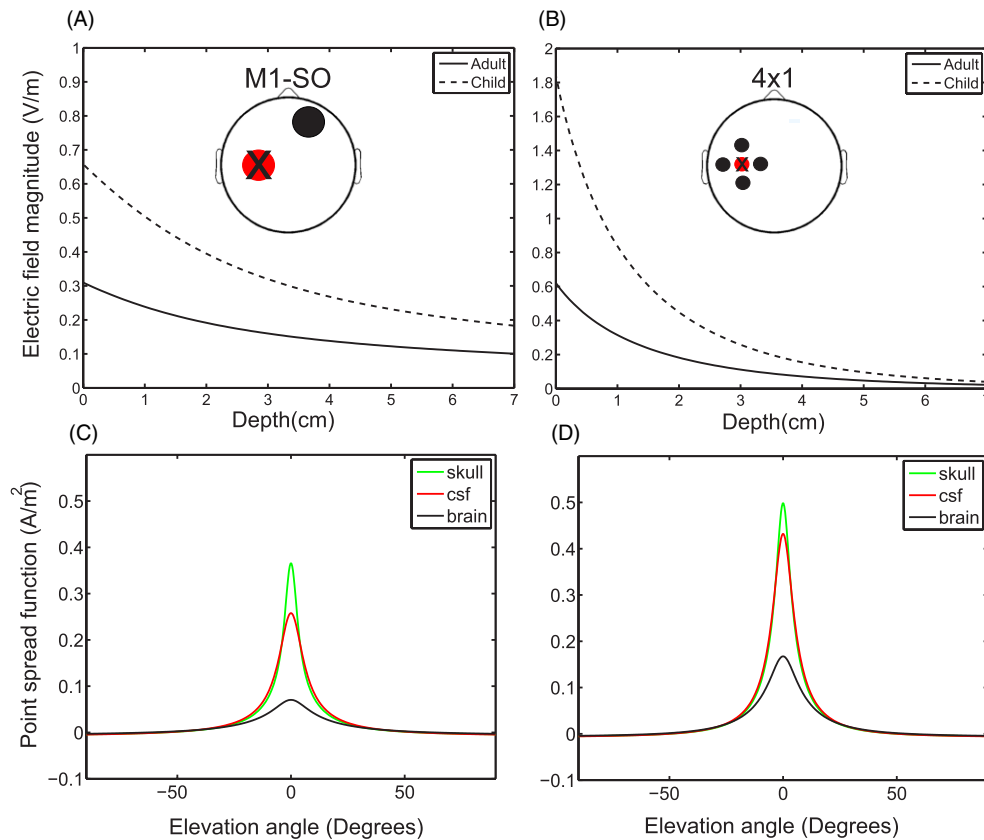
Figure 4. The electric fields induced by two montages in the heads of an adult and a child. In the case of the M1-SO montage with large electrodes (A), the electric field magnitude at the surface of the child brain (directly below the anode) is approximately double that at the surface of the adult brain. For the more focal 4×1 montage (B), there is a threefold increase in the electric field induced on the child's cortical surface. These differences may be attributed to reduced thicknesses of the skull and CSF layers (in the child), whose effects on current flow are represented by the corresponding PSFs of the adult (C) and child (D) heads.

$(0.65 \text{ V m}^{-1}$ versus $0.31 \text{ V m}^{-1})$. For the 4×1 configuration, there is a threefold increase of the field magnitude in the child brain relative to the adult (1.8 V m^{-1} versus 0.6 V m^{-1}). In both cases, the relative increase in intensity is tapered as one looks deeper into the brain volume. The amount of current impinging on the brain of the child is thus significantly greater and may be attributed to proportional decreases in the thicknesses of the skull (4.8% of the head radius in the adult, 2.8% of the head radius in the child) which attenuates current flow and the CSF (3.3% and 1.6% of head radius in the adult and child, respectively), which diffuses the current passed through the skull layer. Indeed, panels C and D depict the PSFs of the adult and child head, respectively. At the CSF, the child PSF peaks at 0.43 A m^{-2}, compared to 0.26 A m^{-2} in the adult. On the brain surface, the child PSF exhibits a peak of 0.17 A m^{-2}, compared to 0.07 A m^{-2} in the adult.

4.5. Modeling the effect of electrode separation

A common belief amongst tCS practitioners is that to maximize current flow in the brain, one should maximize the separation between the anode and the cathode, as this presumably
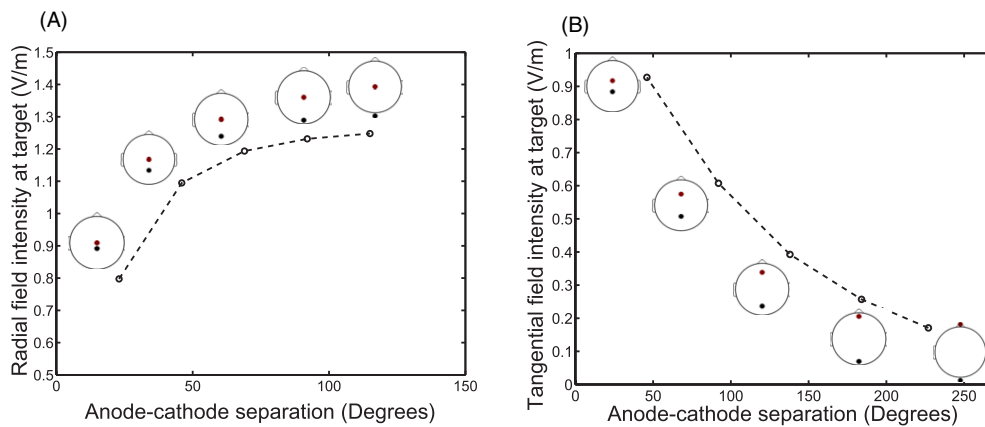
Figure 5. The effect of the separation between anode and cathode on the radial (A) and tangential (B) components of the electric field at the target, which is situated directly below electrode Cz, or the vertex of the brain. Radial current flow is maximized with a maximally distant cathode (i.e. at Iz). On the other hand, maximally intense tangential current flow is achieved with minimal separation between anode and cathode (i.e. anode at FCz and cathode at FPz).

minimizes the amount of current shunted through the scalp. Here, we explored the effect of the separation between anode and cathode on the electric field intensity achieved at the target, which was assumed to lie at the vertex of the brain—directly below electrode Cz—without loss of generality. Circular 'high-definition' electrodes with a diameter of 12mm were modeled. We treat the cases of radial and tangential stimulation separately: in the case of a desired radial current flow, the anode was fixed to Cz, while the cathode was varied along the midline from position CPz to Iz. This simulation setup was motivated by the findings of Dmochowski *et al* (2011), where optimal radial stimulation resulted from placing the anode directly above the target. On the other hand, it was also shown by Dmochowski *et al* (2011) that the optimization of stimulation in the tangential direction leads to the electrodes being placed on either side of the target. Thus, in the case of desired tangential current flow, the locations of the electrodes here were chosen such that the target is equidistant to the anode and the cathode, with the separation between electrodes varying according to Nz/Iz, FPz/Oz, AFz/POz, Fz/Pz and FCz/FPz.

Figure 5 displays the radial (A) and tangential (B) components of the electric field as a function of the angular separation between the anode and the cathode. It is immediately apparent that when desiring radial current flow at the target, one should indeed place the return electrode at the maximally distant location. Less obvious are the results of panel B, which conveys that for maximally intense tangential stimulation, the spacing between anode and cathode should be *minimized*.

5. Optimization of applied current

The locations of the electrodes are a key parameter in tCS design. Indeed, the 'backward problem'—given a desired electric field, to determine the montage which best approximates that field—has been the subject of recent investigation (Dmochowski *et al* 2011, Im *et al* 2008). In this section, we show how the applied surface current $J(\theta, \phi)$ may be optimized to target a desired brain area. Recall from (13) that given an electric potential distribution specified in

the frequency domain by $A_{lm}^{(1)}$, the scalp current density which generates this potential field is simply $\frac{A_{lm}^{(1)}}{[\mathbf{G}_l]_{1,7}}$. The resulting montage, assuming that it exists and is finite, yields precisely the electric field described by $A_{lm}^{(1)}$.

Instead of working with the potential, we instead optimize the radial component of the electric field in the brain at a target depth R_o, which is given by

$$-\left(\frac{\partial V_1}{\partial r}\right)_{r=R_o} = -\sum_{l=0}^{\infty}\sum_{m=-l}^{l} A_{lm}^{(1)} l R_o^{l-1} Y_{lm}(\theta, \phi). \tag{20}$$

Ideally, we would like the radial component of the electric field to approximate a delta Dirac function:

$$-\left(\frac{\partial V_1}{\partial r}\right)_{r=R_o} = \frac{\delta(\theta - \theta_o)\delta(\phi - \phi_o)}{\sin\theta}, \tag{21}$$

where the denominator is included such that the resulting delta function integrates to one across the surface of a unit sphere. From (6), it follows that the Fourier transform of (21) is given by

$$\delta_{lm} R_o^l = Y_{lm}^*(\theta_o, \phi_o). \tag{22}$$

Connecting (20) to (22), we identify that in order to achieve an idealized electric field with a focal direction of (θ_o, ϕ_o) at depth R_o, one requires

$$A_{lm}^{(1)} = \frac{-Y_{lm}^*(\theta_o, \phi_o)}{l R_o^{l-1}}. \tag{23}$$

From (15), we obtain the scalp current that achieves this idealized field as

$$J_{lm} = \frac{-Y_{lm}^*(\theta_o, \phi_o)}{[\mathbf{G}_l]_{1,7} \, l R_o^{l-1}}. \tag{24}$$

Transforming back into the space domain, the idealized montage is written as

$$J(\theta, \phi) = -\sum_{l=0}^{\infty}\sum_{m=-l}^{l} \left([\mathbf{G}_l]_{1,7} \, l R_o\right)^{-1} (R_4/R_o)^l Y_{lm}^*(\theta_o, \phi_o) Y_{lm}(\theta, \phi). \tag{25}$$

Thus, by implementing the montage of (25), the radial component of the electric field at a depth of R_o follows a delta-Dirac distribution, with asymptotic density at the specified angle (θ_o, ϕ_o), and zero density elsewhere. In practice, this optimized field may only be approximated by truncating the spherical harmonic expansion at a finite value for l.

Figure 6(a) displays optimal montages corresponding to the expansions of (25) truncated up to spatial frequencies of 5, 10, 20 and 30 cycles/degree. The selected target was $\theta = \phi = 0$. The resulting montages exhibit an azimuthal symmetry, thus allowing us to plot the optimized current density as a one-dimensional function of the elevation θ. From the figure, it follows that the optimally focal montage takes the form of a spherical 'sinc' function. This is a satisfying result, as it confirms the findings of Datta *et al* (2009), which revealed that the 4×1 configuration, consisting of a central anode and four surrounding cathodes, yielded superior focality over conventional montages. The 4×1 configuration may be viewed as a low-order approximation of the spherical sinc. The electric field corresponding to the spherical sinc montage approximates a delta-Dirac function, as displayed for increasing spatial bandwidth in figure 6(b). Figures 6(c) and (d) display the optimally focal montage and resulting electric field on the surfaces of the corresponding spheres for bandwidths of 5 and 30 cycles/π, respectively. Due to the azimuthal symmetry, the spherical sinc montage translates to concentric rings of alternating polarity, while the resulting electric field approximates a two-dimensional delta-Dirac function. At a bandwidth of 5 cycles/π, the resulting montage consists of few
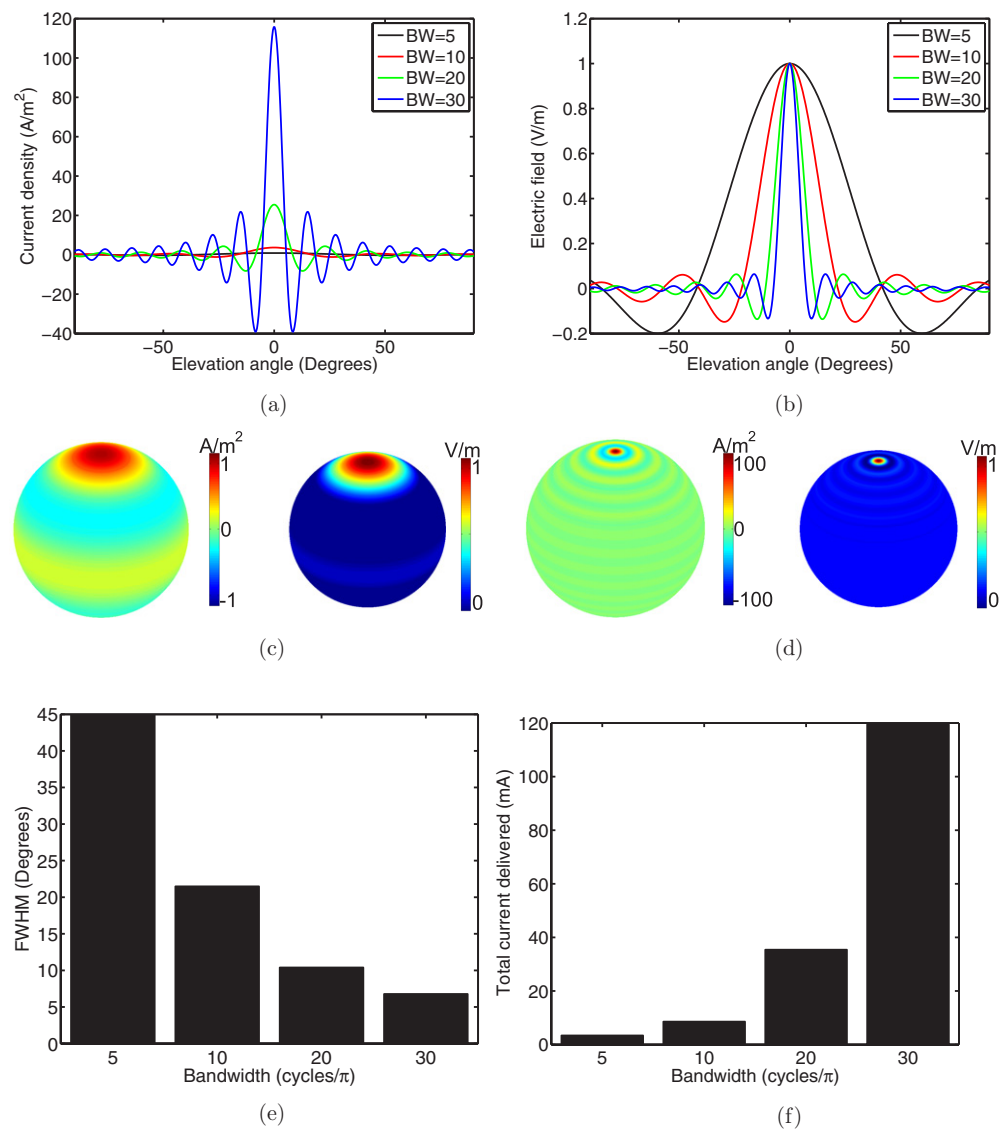
Figure 6. The optimal montage for targeting an infinitesimal point on the cortical surface takes the form of a spherical 'sinc' function (a), resulting in an electric field whose radial component approximates a delta-Dirac function (b). The optimal montage and resulting field are depicted on the surface of their respective spheres for BW = 5 (c) and BW = 30 (d). Expanding the bandwidth (increasing the order) of the spherical harmonic expansion leads to a more focal electric field (e), but at the expense of increased input current (f). (a) Optimal current distribution, (b) optimal electric field, (c) 'scalp' current (left) and 'brain' electric field (right) for BW = 5, (d) 'scalp' current (left) and 'brain' electric field (right) for BW = 30, (e) focality and (f) current delivered.

rings of relatively low magnitude while yielding limited focality. On the other hand, at 30 cycles/π, both the number of rings and the magnitude increases dramatically, resulting in a highly concentrated field, albeit at extremely high current requirements. From figure 6(e), the corresponding FWHM decreases as we include higher order terms in (25). This increased

focality, however, comes as the expense of increasing required current levels, as shown in figure 6(f). Thus, safety considerations are a limiting factor in tCS focality: to yield the electric field cancelation (around the target) necessary to produce a narrow focal region, high input current levels are required. At the range of commonly applied dosages (i.e. 2 mA), the corresponding FWHM is 45°, or a quarter of the distance from $\theta = 0$ to $\theta = \pi$.

6. Discussion

In presenting this work, we hope to have provided an easily accessible tool which can be used by tCS researchers and clinicians to explore various stimulation parameters. While the mathematical details may be elusive to some readers, we are making the complete source code used in the generation of the results available online via a graphical user interface (neuralengr.com/spheres). We believe that while numerical methods such as FE solvers are essential in developing forward models for individualized heads, the use of such tools somewhat prevents us from gaining insight and inferring general principles of transcranial current flow. For example, we have shown (figure 2) that the human head is a spatial low-pass filter with an easily-computable frequency response (similar results have been previously derived in the context of electroencephalography (Srinivasan *et al* 1998)). Moreover, the eigenfunctions of the head are the spherical harmonics: this means that if the input scalp current takes the form of $Y_{lm}(\theta, \phi)$, the resulting potential in the brain is simply a scaled version of this basis function! Here, the simplicity of the frequency–domain approach is most evident, as numerical methods are surely not needed to carry out a multiplication operation. Of course, the montages employed in practice are linear combinations of these harmonics; in this case, the forward model is given by a weighted summation of the basis functions $Y_{lm}(\theta, \phi)$.

By transforming the frequency–domain relationship between the applied scalp current and the generated electric field back into the space domain, we derived the PSF of the head, which quantifies the attenuation and blurring posed by the volume conductor to a unit current placed on the scalp: the current density peaks at 0.45, 0.33 and 0.18 A m^{-2} on the surfaces of the skull, CSF and brain, respectively. Meanwhile, the corresponding FWHMs are 10°, 18° and 26°, respectively (figure 2). The impact of the CSF is further elucidated when omitting the CSF layer from the head model: in this case, the brain current peaks at 0.28 A m^{-2}, with the FWHM decreasing to 20°.

We then utilized our model to investigate the effects of electrode size on the induced electric field in the brain: it was revealed that smaller (5 cm^2) electrodes yield an electric field that is 60% more intense and 41% more focal compared to larger (5 cm^2) electrodes (figure 3). Next, we contrasted the fields induced by conventional montages in the adult versus child brains: the induced field strength was found to be double and triple in the child for the M1-SO and 4×1 configurations, respectively (figure 4). It was also shown that the issue of electrode separation requires a determination on whether the desired current flow at the target is radial or tangential: when radial flow is sought, maximal anode–cathode separation was found to be optimal (figure 5). On the other hand, a minimal anode–cathode separation was found to maximize the tangential component of the induced electric field at the target (figure 5). This result extends previous findings showing that while the anode–cathode separation generally increases the magnitude of current flow in the brain (Datta *et al* 2010), multiple factors such as montage type and as desired orientation may determine optimal electrode separation in clinical settings. For example, Moliadze *et al* (2010) found a negative correlation between electrode separation and tCS induced after-effects. Finally, we showed that the optimal montage for targeting an infinitesimal point on the brain takes the form of a spherical sinc function, with

concentric rings of alternating polarity around the target (figure 6). The resulting field may be taken to be as focal as desired, but at the expense of increasingly unsafe current levels.

6.1. Spherical harmonics and numerical stability

Working in the spherical harmonic domain is not without its caveats. The associated Legendre polynomials take on very large values as the spatial frequency exceeds $\approx$20 cycles/π. The matrix $\mathbf{H}_l$, while inherently badly scaled for $l \geqslant 5$, was inverted up to $l = 140$ on a standard microprocessor. At $l \geqslant 140$, the matrix is singular to working precision. However, from figure 2, note that the frequency response values at such high frequencies are negligibly small. Therefore, for practical use, we anticipate that a bandwidth of 30–50 cycles/π will suffice for most tCS analyses. For example, figures 3–6 were constructed using a bandwidth of 50 cycles/π. Higher order frequency components are required to approximate sharp edges such as the boundary of an electrode.

6.2. Tangential current flow

In deriving the PSF of the head (via the inverse Fourier transform of the frequency response), we have related the applied scalp current (oriented normally to the head) to the radial component of the resulting current flow. This computation was facilitated by the fact that the radial derivative of a spherical harmonic expansion is itself straightforward to express as a spherical harmonic expansion. On the other hand, it is not easy to express the derivative of a spherical harmonic expansion with respect to the elevation angle θ in terms of the basis functions $Y_{lm}(\theta, \phi)$. As a result, the derivation of the PSF between the scalp current and the tangential component of the induced current flow is yet undetermined and the subject of ongoing work. While explicit computation of the tangential PSF has proved elusive, it should be pointed out that the frequency response $G_l^{(1)}$ allows for the computation of the electric field (and thus current density) in *any* direction by taking the gradient of the electric potential V_1.

6.3. Electrode shape

In this paper, we have derived the spherical harmonic expansions of both point and circular electrodes. Other electrode shapes, for example rectangular pads, may be expressed in the frequency domain by integrating the basis function $Y_{lm}^*(\theta, \phi)$ across the electrode's extent. Once the expansion of one such electrode is determined, all rotations of this nominal electrode along the sphere may be determined using the convenient rotation property of the spherical harmonics (see the appendix).

6.4. Additional shells

While we have restricted the head model to four shells, it is straightforward to extend the linear system of (12) to encompass additional tissue layers. For example, a fifth shell may be inserted between the skull and the scalp to model the effect of subcutaneous fat. In the limiting case, the matrix $\mathbf{H}_l$ becomes infinite, with the 'head' model consisting of an infinite number of infinitesimally thin concentric shells.

6.5. Spherical models in rational tCS design

The rational development of tCS therapies requires not simply modeling as many montages on as many subjects as possible, but rather deriving general rules for dose design. To that end,

spherical models serve as an important starting point whose predictions may then be verified in more complex models. Note that with MRI-based models, it is difficult to vary one parameter while holding the others fixed: for example, increasing electrode separation also changes local skull thickness. This is further complicated when considering montage changes across subjects (e.g. increasing electrode separation in an adult versus a child). In addition, MRI-derived forward models often yield detailed patterns of current flow, thus making it difficult to draw general conclusions and interpret predictions. Spherical models are advantageous in this regard; furthermore, sweeping a multi-dimensional parameter space becomes feasible with the closed-form technique presented here. Finally, from a pragmatic standpoint, current MRI-based approaches are not easily accessible, and we propose that the framework presented here may serve as a valuable tool to inform ongoing tCS clinical trials.

Acknowledgments

Appendix. Spherical harmonic expansion of a circular electrode

We wish to derive the spherical Fourier transform of a spherical cap (Harris *et al* 1998) on a sphere of radius R. Without loss of generality, we assume that the center of the cap is at $\theta = \phi = 0$, meaning that the corresponding function exhibits azimuthal symmetry:

$$p(\theta, \phi) = p(\theta) = \begin{cases} 1 & 0 \leqslant \theta \leqslant \psi \\ 0 & \theta \geqslant \psi. \end{cases} \tag{A.1}$$

The spherical harmonic coefficients of this function are given by

$$\begin{aligned} P_{lm}R^l &= \int_0^{2\pi} \int_0^{\pi} p(\theta, \phi) Y_{lm}^*(\theta, \phi) \sin\theta \, d\theta \, d\phi \\ &= \sqrt{\frac{2l+1}{4\pi} \frac{(l-m)!}{(l+m)!}} \left(\int_0^{2\pi} e^{im\phi} \, d\phi \right) \left(\int_0^{\psi} P_{lm}(\cos\theta) \sin\theta \, d\theta \right) \\ &= \sqrt{\frac{2l+1}{4\pi} \frac{(l-m)!}{(l+m)!}} \, (2\pi \delta_{m0}) \left(\int_0^{\psi} P_{lm}(\cos\theta) \sin\theta \, d\theta \right) \\ &= \sqrt{\pi(2l+1)} \int_{\cos\psi}^{1} P_{l0}(x) \, dx, \end{aligned} \tag{A.2}$$

where in the third line we have made use of the Kronecker delta function: $\delta_{m0} = \begin{cases} 1 & m=0 \\ 0 & \text{otherwise.} \end{cases}$ As the associated Legendre polynomials are easily integrable, the integral in (A.2) may be evaluated either in the closed form (for every desired order l) or numerically. Note that the coefficients are independent of the degree m. The resulting function models an electrode at the vertex of the head (i.e. Cz) and has a surface area specified by the parameter ψ.

In order to compute the coefficients for an arbitrary electrode position $(\theta, \phi) = (\beta, \alpha)$, one can utilize the rotation property of the spherical harmonics (Wigner *et al* 1931): the coefficients of the rotated function $q(\theta, \phi) = p(\theta - \beta, \phi - \alpha)$ may be computed as a transformation of the original coefficients P_{lm},

$$Q_{lm}R^l = \sum_{m'=-l}^{l} e^{-jm'\alpha} d_{mm'}^l(\beta) \left(P_{lm'}R^l \right), \tag{A.3}$$

where

$$d^l_{mm'}(\beta) = \left[(l+m')!(l-m')!(l+m)!(l-m)!\right]^{1/2}$$
$$\times \sum_s \frac{(-1)^{m'-m+s}}{(l+m-s)!s!(m'-m+s)!(l-m'-s)!}$$
$$\times \cos(\beta/2)^{2l+m-m'-2s} \sin(\beta/2)^{m'-m+2s}, \quad\quad (A.4)$$

where the summation over s in (A.4) is such that the arguments of all factorials are non-negative.

In our development, we implemented the transformation of (A.3) directly, resulting in numerical stability up to $l = 140$. If it is desired to model arbitrarily located circular electrodes with even higher frequency components, one may choose to implement the method of Gimbutas and Greengard (2009), which reduces the computational time and alleviates the numerical stability issues associated with the naïve approach.

References

Brunoni A R *et al* 2012 Clinical research with transcranial direct current stimulation (tDCS): challenges and future directions *Brain Stimulation* **5** 175–95

Chatrian G E, Lettich E and Nelson P L 1985 Ten percent electrode system for topographic studies of spontaneous and evoked EEG activity *Am. J. EEG Technol.* **25** 83–92

Datta A, Bansal V, Diaz J, Patel J, Reato D and Bikson M 2009 Gyri-precise head model of transcranial dc stimulation: improved spatial focality using a ring electrode versus conventional rectangular pad *Brain Stimulation* **2** 201–7

Datta A, Rahman A, Scaturro J and Bikson M 2010 Electrode montages for tDCS and weak transcranial electrical stimulation Role of 'return' electrode's position and size *Clin. Neurophysiol.* **121** 1976–8

Dmochowski J P, Datta A, Bikson M, Su Y and Parra L C 2011 Optimized multi-electrode stimulation increases intensity and focality at target *J. Neural Eng.* **8** 046011

Driscoll J R and Healy D M 1994 Computing Fourier transforms and convolutions on the 2-sphere *Adv. Appl. Math.* **15** 202–50

Gimbutas Z and Greengard L 2009 A fast and stable method for rotating spherical harmonic expansions *J. Comput. Phys.* **228** 5621–7

Griffiths D J 1999 *Introduction to Electrodynamics* (Upper Saddle River, NJ: Prentice-Hall)

Harris J W and Stocker H 1998 Spherical segment (spherical cap) *Handbook of Mathematics and Computational Science* (New York: Springer) p 107 section 4.8.4

Holdefer R N, Sadleir R and Russell M J 2006 Predicted current densities in the brain during transcranial electrical stimulation *Clin. Neurophysiol.* **117** 1388–97

Im C W, Jung H H, Choi J D, Lee S Y and Jung K Y 2008 Determination of optimal electrode positions for transcranial direct current stimulation *Phys. Med. Biol.* **53** N219–25

Jackson J D 1975 *Classical Electrodynamics* (New York: Wiley)

Minhas P *et al* 2010 Electrodes for high-definition transcutaneous dc stimulation for applications in drug delivery and electrotherapy, including tDCS *J. Neurosci. Methods* **190** 188–97

Miranda P C, Faria P and Hallett M 2009 What does the ratio of injected current to electrode area tell us about current density in the brain during tDCS? *Clin. Neurophysiol.* **120** 1183–7

Miranda P C, Lomarev M and Hallett M 2006 Modeling the current distribution during transcranial direct current stimulation *Clin. Neurophysiol.* **117** 1623–9

Moliadze V, Antal A and Paulus W 2010 Electrode-distance dependent after-effects of transcranial direct and random noise stimulation with extracephalic reference electrodes *Clin. Neurophysiol.* **121** 2165–71

Nitsche M A, Doemkes S, Karakse T, Antal A, Liebetanz D, Lang N, Tergau F and Paulus W 2007 Shaping the effects of transcranial direct current stimulation of the human motor cortex *J. Neurophysiol.* **97** 3109–17

Nitsche M A and Paulus W 2000 Excitability changes induced in the human motor cortex by weak transcranial direct current stimulation *J. Physiol.* **527** 633–9

Nitsche M A *et al* 2008 Transcranial direct current stimulation: state of the art 2008 *Brain Stimulation* **1** 206–23

Nunez P L and Srinivasan R 2006 *Electric Fields of the Brain: The Neurophysics of EEG* (New York: Oxford University Press)

Peterchev A V *et al* 2011 Fundamentals of transcranial electric and magnetic stimulation dose: definition, selection, and reporting practice *Brain Stimulation* (at press) doi:10.1016/j.brs.2011.10.001

Priori A 2003 Brain polarization in humans: a reappraisal of an old tool for prolonged non-invasive modulation of brain excitability *Clin. Neurophysiol.* **114** 589–95

Srinivasan R, Tucker D and Murias M 1998 Estimating the spatial Nyquist of the human EEG *Behav. Res. Methods* **30** 8–19

Stecker M M 2005 Transcranial electric stimulation of motor pathways: a theoretical analysis? *Comput. Biol. Med.* **35** 133–55

Wagner T, Fregni F, Fecteau S, Grodzinsky A, Zahn M and Pascual-Leone A 2007 Transcranial direct current stimulation: a computer-based human model study *Neuroimage* **35** 1113–24

Wigner E P 1931 *Gruppentheorie und ihre Anwendungen auf die Quantenmechanik der Atomspektren* (Braunschweig: Vieweg)